# Chapter 2
# Methods

## 2.1 Synthesis and Characterization of Silica Nanoparticles

### *2.1.1 Synthesis*

Silica nanoparticles of diameter 12, 21 and 42 nm were prepared by the hydrolysis of tetraethyl orthosilicate $Si(OC_2H_5)_4$ (TEOS) with water. The reaction taking place is a sol-gel process and is shown below:

$$Si(OC_2H_5)_4 + 2H_2O \rightarrow SiO_2 + 4C_2H_5OH$$

The reaction proceeds by hydrolysis of TEOS to $Si(OH)_4$ and a series of condensation reactions that convert the orthosilicic acid into a mineral-like solid via the formation of Si-O-Si linkages [1]. Reaction was carried out in the presence of the basic amino acid lysine as reported by Davis et al. [2] and Thomassen et al. [3] In a typical synthesis 0.51 g of lysine monohydrate was dissolved in 102 mL milli-Q water in a 250 mL round bottom flask (RB). After equilibration at 60 °C for 1 h, 16 mL of TEOS was added dropwise and the reaction mixture was kept in the reaction vessel at an optimized temperature and stirring rate. The resulting silica dispersion was dialyzed to remove unreacted TEOS and reaction by-products, using dialysis membranes with a molecular-weight cut-off at 14 kDa. Dialysis was carried for 1 week with changing of milli-Q water twice per day. Bigger aggregates of silica formed during the reaction were removed from the dialyzed dispersion by a series of filtration steps. Filtration was done with 5 μm followed by 0.8 μm and eventually using 0.22 μm filters. In order to avoid aggregation of silica, pH was adjusted to ≃9 and the dispersion was stored at 8 °C. The particle size was tuned solely by optimizing the stirring speed and the adjustment of the temperature of the reaction mixture. Since the different sizes of silica nanoparticles were prepared by altering only the physical conditions, the surface chemistry (surface charge density) presumably remains unaltered. The resulting silica nanoparticles were characterized for their size and polydispersity by Small Angle X-ray Scattering (SAXS), for their surface charge by zeta potential and for their specific surface area by nitrogen adsorption.

B. Bharti, *Adsorption, Aggregation and Structure Formation in Systems of Charged Particles*, Springer Theses, DOI: 10.1007/978-3-319-07737-6_2,

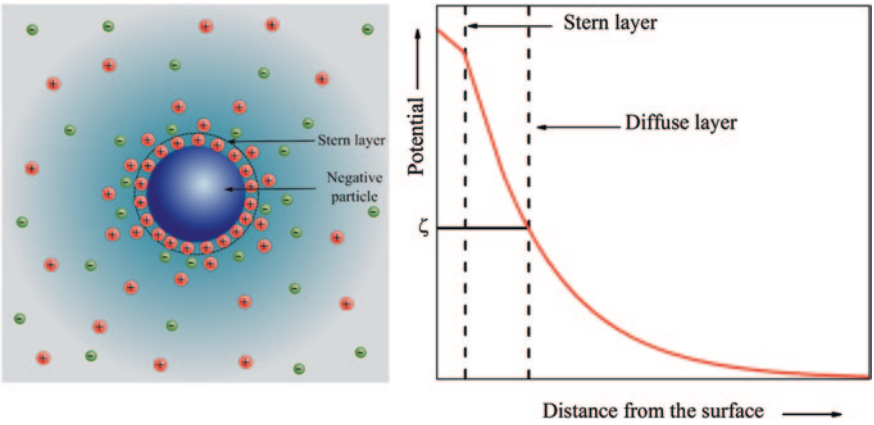


**Fig. 2.1** Diagram showing the distribution of the ions around the negatively charged particle, indicating the presence of a shell of strongly bound counter ions (stern layer) and weakly bound layer called the diffuse layer

### *2.1.2 Zeta Potential*

The surface charge of a colloidal particle in aqueous media is balanced by an equal number of oppositely charged counter ions. Some of the counter ions are bound to the surface within, the so called *Stern* or *Helmholtz layer*, while others form an atmosphere of loosely bound ions further away from the surface known as the *diffuse double layer* [4]. Within the diffuse layer there is a notional boundary, inside which the ions move together with the particle, whereas the ions outside this boundary do not travel with the particle. This boundary is called the surface of hydrodynamic shear or *slipping plan* [5] (Fig. 2.1). The potential that exists at this boundary is known as the *zeta potential*. It is an electric potential in the interfacial double layer at the location of the slipping plane versus a point in the bulk fluid away from the interface [6]. In other words, zeta potential is the potential difference between the bulk dispersion medium and the stationary layer of fluid attached to the particle's surface. Zeta potential is not measurable directly but it can be calculated from electrophoretic mobility ($\mu_e$) using the Henry equation

$$\zeta = \frac{3\eta\mu_e}{2\varepsilon f(\kappa R)}, \tag{2.1}$$

where $\zeta$ is the zeta potential of the particle with radius $R$, $\eta$ and $\varepsilon$ are the viscosity and dielectric constant of the medium respectively and $f(\kappa R)$ is called the Henry's function. The Henry's function depends on particle size and the ionic strength of the dispersion via the Debye length ($1/\kappa$)

$$1/\kappa = \sqrt{\frac{\varepsilon_0 \varepsilon k_B T}{2N_A e^2 I}} \tag{2.2}$$

where $\varepsilon_0$ is the permittivity of free space, $\varepsilon$ is the Dielectric constant, $k_B$ is Boltzmann constant; $T$ is the temperature in K, $N_A$ being the Avogadro number, $e$ is the elementary electronic charge and $I$ is the ionic strength of the dispersion.

The electrophoretic mobility of a particle can be determined by the application of an electric field across the dispersion. The charged particles suspended in the electrolyte are attracted towards the electrode of opposite charge. Viscous forces acting on the particles tend to oppose this movement. When a steady velocity $v$, is reached, the electrophoretic mobility is given by $\mu_e = v/E$, where $E$ is the electric field strength. The Henry's function $f(\kappa R)$ acquires the value of 1.5 in the limit $\kappa R \gg 1$, i.e. large particles and high ionic strength (Smoluchowski approximation), whereas $f(\kappa R) = 1$ in the limit $\kappa R \ll 1$, i.e. small particles in low ionic strength media (Hückel approximation). Measurements of the electrophoretic mobility were carried out with a Zetasizer Nano ZS (Malvern Instruments, UK) operating with a 4 mW HeNe laser (633 nm) and a light scattering detector positioned at 90° and a temperature control jacket for the cuvette. The sample was equilibrated for 2 min at 25 °C before starting the measurements. Three measurements, each consisting of 30 runs were performed for each sample, and an average of the measurements was used for further reference.

### 2.1.3 Nitrogen Adsorption

The surface area of the nanoparticles was determined by nitrogen adsorption at 77 K. The adsorption isotherm was then interpreted on the basis of BET model of multilayer gas adsorption [7]. The surface of a solid is regarded as an array of equivalent adsorption sites. As in *Langmuir* model of monolayer adsorption, each of these sites can accommodate one adsorbed molecule in direct contact with the surface. However, in BET model each occupied site can act, in turn as a site for molecules adsorbed in the second layer, and so on for infinite number of higher layers. The resulting BET model can be written in the form

$$\frac{p/p_0}{V(1-p/p_0)} = \frac{1}{V_m c} + \frac{c-1}{V_m c}(p/p_0) \tag{2.3}$$

here $V$ is the amount of adsorbed gas expressed as ideal gas volume at standard temperature and pressure ($V_{STP}$), $V_m$ is respective volume of a complete monolayer adsorbed gas quantity, $p$ is the equilibrium pressure, $p_0$ is saturation vapor pressure, the term $p/p_0$ is called the relative vapor pressure and $c$ is the BET constant, $c = e^{\Delta E/RT}$, where $\Delta E$ is the difference between the heat of adsorption of first layer and the higher layers. The derivation of the BET equation can be found elsewhere [7]. The relation presented in Eq. 2.3 can be plotted with $\frac{p/p_0}{V(1-p/p_0)}$ as ordinate and $p/p_0$ as abscissa resulting into a straight line. This representation is called BET plot. In many cases, the linear behavior of the equation is maintained for $0.05 < p/p_0 < 0.3$. The slope of the straight line is equal to $1/V_m$ and is related to the specific surface area ($a_s$) by the following relation

$$a_s = \frac{a_m V_m N_A}{V_{STP}} \tag{2.4}$$

where $a_m$ is the average area occupied by a molecule of adsorbate ($a_m = 0.162$ nm$^2$ for $N_2$), $N_A$ is the Avogadro constant and $V_{STP}$ is the volume occupied by 1 mol of the gas at STP ($V_{STP} = 22.414$ L/mol). In our work, we have measured the adsorption isotherms of nitrogen at 77 K for the synthesized silica materials by gas volumetry using a Micromeritics Gemini III 2,375 Volumetric Surface Analyzer. Before the gas adsorption measurements, the silica material was dried and outgassed at 393 K for 1 h under vacuum. For nitrogen adsorption isotherm measurements, Micromeritics sample holder with thermal isolation by Dewar vessel containing liquid nitrogen was used.

## 2.2 Adsorption at Solid/Liquid Interface

Adsorption phenomena take place whenever two immiscible phases are brought into direct contact with each other, resulting in the excess accumulation of either component in the interfacial region. The process of transfer of the component from bulk to the surface continues until a state of adsorption equilibrium is reached [8]. Adsorption from solution onto a solid surface depends on the composition of the solution and is expressed in terms of an *adsorption isotherm,* where amount adsorbed ($n_{ads}$) is expressed as the function of equilibrium concentration (i.e. free adsorbate concentration) in the bulk ($c_{eq}$). In our studies, we determined adsorption isotherms by solvent depletion method. In a typical experimental scheme, a certain concentration of adsorbate ($c_0$) (protein or surfactant) was added to the dispersion containing a fixed amount of silica nanoparticles and the mixture obtained was equilibrated for 24 h on a multiple axel rotor. After complete equilibrium was reached, nanoparticles with the adsorbed protein (or surfactant) were removed from the dispersion by centrifugating the samples for 2 h at ≃21,000 g (15,000 RPM) in a Hettich Universal 320R centrifugation equipment fitted with 1420-A sample holder. The supernatant was carefully isolated from the centrifugated mixture and the amount of unadsorbed protein (or surfactant) in the supernatant was determined by the methods described in the following sections. After the precise determination of the residual equilibrium concentration $c_{eq}$ the amount adsorbed was calculated as $n_{ads} = V(c_0 - c_{eq})$, where $V$ is the volume of dispersion and $c_0$ is the total amount of adsorbent added to silica dispersion. The surface concentration (excess) of the adsorbed material is then given by Eq. 2.5 [9, 10]

$$\Gamma = \frac{(c_0 - c_{eq})V}{a_s m} \tag{2.5}$$

here $\Gamma$ is the surface excess concentration (expressed in mol/m$^2$), $c_0$, $c_{eq}$ are the concentration before and after equilibration with the solid (in mol/L), $V$ is the total

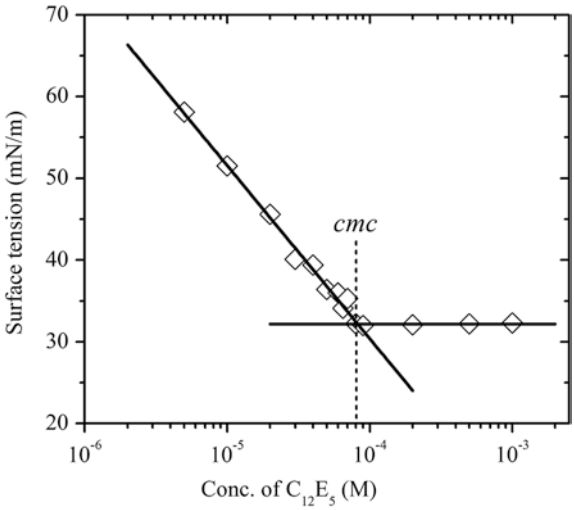


**Fig. 2.2** Surface tension variation of aqueous solution of $C_{12}E_5$ surfactant at different bulk concentrations, the intersection point of the linear fit for the two regions of surface tension *curve* gives the value of *cmc*

volume of solution (in L), $m$ is the total mass (in g) and $a_s$ is the specific surface area of the particles (in $m^2/g$) (Sect. 2.1.3). Different initial amounts of adsorbate ($c_0$) were added to the nanoparticle dispersion in order to access different surface concentration regimes, and thus to obtain complete adsorption isotherm.

### *2.2.1 Surfactant Adsorption*

The adsorption isotherm of $C_{12}E_5$ on silica nanoparticles was determined by the procedure explained in the previous section. Surface tension was used to determine the equilibrium surfactant concentration ($c_{eq}$). Surface tension measurements were made by the Du Noüy ring method using a Krüss K11 Tensiometer. The Platinum-Iridium ring of 20 mm diameter was used to examine the pulling force (and hence surface tension) from the liquid-air interface for the determination of surface tension of solution. The ring was completely dried before each measurement and all the samples were equilibrated at 25 °C for 5 min before the measurement. Three consecutive readings were taken and their mean value was used as the final surface tension of the solution. A surface tension curve for known concentration of $C_{12}E_5$ surfactant is shown in Fig. 2.2, the dashed line indicates the value of critical micelle concentration (*cmc*). The region of linear decay in the surface tension with surfactant concentration < *cmc*, was used as the reference, and the linear fit to the points was used as the calibration values for determining unknown concentrations of surfactant. A typical adsorption isotherms curve for nonionic surfactant ($C_{12}E_5$) on silica surface is shown in Fig. 2.3a. The adsorption isotherm of nonionic surfactants on silica surface shows an S-shaped curve [11, 12] which is contradistinct from the *Langmuir* model of adsorption (Fig. 2.3b).

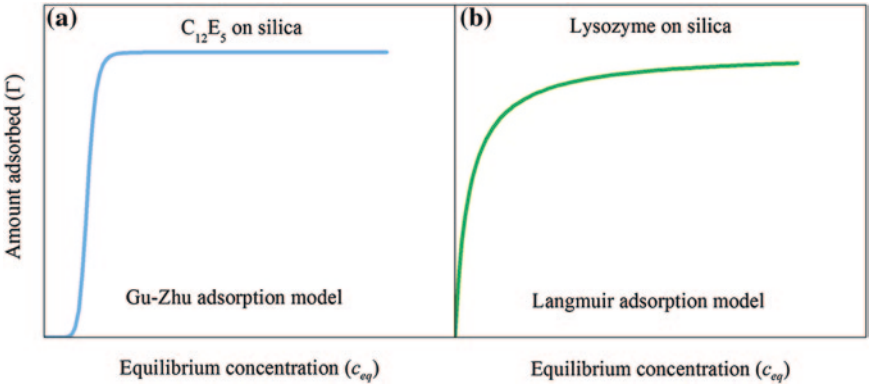


**Fig. 2.3** Generalized example of two different types of adsorption isotherms on silica nanoparticles. **a** Adsorption isotherm of $C_{12}E_5$ on silica, it presents an S-type curve and can be represented by Gu-Zhu model [14]. **b** Lysozyme adsorption isotherm at silica surface, it shows a very strong affinity of adsorption on silica surface and can be represented by Langmuir adsorption model

For nonionic ethoxylate surfactants, because of the presence of weak non-electrostatic interactions between the ethoxylate surfactant head groups and silica surface silanol groups, the adsorption isotherms do not show the second plateau region as is the case with ionic surfactants [13] (not shown here). The adsorption behavior of nonionic surfactant has been well explained by Zhu et al. [14]. According to the proposed model, the aggregation of $n$ monomers of nonionic surfactant on a surface site ($s$) forms a surface-micelle, where $n$ is the nominal aggregation number of the surface-micelle.

At equilibrium,

$$s + n\text{-monomers} \leftrightarrow \text{surface-micelle}$$

By applying the mass action model to the above assumption, the surface excess concentration ($\Gamma$) of nonionic surfactant is given by the following Eq. 2.6.

$$\Gamma = \frac{\Gamma_m K c_{eq}^n}{1 + K c_{eq}^n} \tag{2.6}$$

where $\Gamma_m$ is the maximum surface concentration, $c_{eq}$ is the equilibrium concentration of surfactant, $K$ is the adsorption constant and $n$ is the mean aggregation number. This equation was used for fitting the experimental data points in (Chap. 4) and hence determining the $\Gamma_m$ and $n$ values.

### 2.2.2 Protein Adsorption

Adsorption isotherms of proteins (lysozyme or cytochrome C) on silica nanoparticles were measured at different pH and ionic strength in 50 mM 2-(N-morpholino)

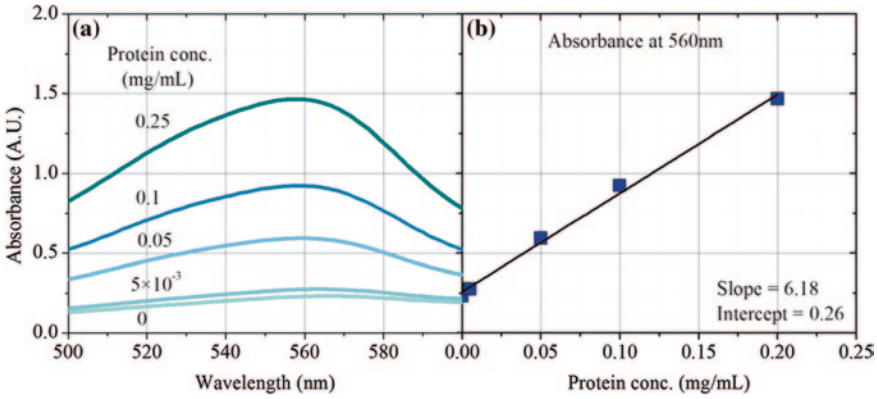


**Fig. 2.4** **a** Absorbance variation for samples treated with BCA protein assay at 60 °C for 2 h and having different protein content indicated by the numbers. **b** The change in the absolute absorbance values at 560 nm; the scattered points are the measured data points (shown in **a**) and *solid line* is the linear fit to the data points

ethanesulfonic acid (MES) or 2-(Bis(2-hydroxyethyl)amino)acetic acid (BICINE) buffer. Organic buffers were used with the purpose of keeping the ionic concentration caused by buffers to a minimum. The free protein concentration in the supernatant obtained after centrifugating out silica with adsorbed protein was determined by measuring its absorbance at $\lambda = 280$ nm using a Varian Cary UV-vis spectrophotometer. For precise determination of protein concentration at pH > 7, the BCA protein assay kit was used. 0.15 ml of the protein sample was incubated with 3 mL of working reagent for 2 h at 60 ± 1 °C, and the absorbance at $\lambda = 560$ nm was measured. BCA uses reduction of $Cu^{+2}$ to $Cu^{+}$ by protein in an alkaline medium (biuret reaction) with the highly sensitive and selective colorimetric detection of $Cu^{+}$ using a unique reagent containing bicinchoninic acid [15]. At first, a calibration curve with known protein amounts was obtained. Based on this calibration curve, the unknown protein concentration was determined. Figure 2.4a shows the typical UV-vis curves measured for different known concentrations of the protein, The calibration curve resulting from the measurements is shown in Fig. 2.4b. The linear fit to the experimental points gives a slope $m$ with an intercept of $b$. Hence equilibrium concentration of protein is given by Eq. 2.7.

$$c_{eq} = \frac{(A_{560} - b)}{m} \tag{2.7}$$

where $A_{560}$ is the absorbance of the assay-protein complex, $b = 0.26$ and $m = 6.18$.

The adsorption isotherms obtained were of the type shown in Fig. 2.4b. This type of isotherm is typical for strong monolayer adsorption and can be represented by the *Langmuir* adsorption model. According to this model there exists equilibrium between empty surface sites ($s$), free particles ($p$) and sites occupied by a single particle ($sp$), i.e. $s + p \leftrightarrow sp$. Surface of protein at any point can be estimated by the above model using the Langmuir equation [16]

$$\Gamma = \frac{\Gamma_m K c_{eq}}{1 + K c_{eq}} \tag{2.8}$$

where $\Gamma$ is the surface (excess) concentration at any point on adsorption isotherm, $\Gamma_m$ is the maximum surface concentration, $c_{eq}$ is the equilibrium concentration in the solution and $K$ is the Langmuir equilibrium constant. Its value depends on the strength of adsorption, i.e., the binding affinity (or energy) of the sorbent to the substrate. Comparing Eqs. 2.6 and 2.8 the only difference between the two model isotherms is the presence of the aggregation number '$n$' in Eq. 2.6, which accounts for rapid increase in adsorption beyond a specific onset concentration.

## 2.3 Turbidity and Analytic Centrifugation

As will be discussed in Chaps. 6 and 7, the samples of silica dispersion containing lysozyme in a pH range 4–9 causes a lysozyme-mediated silica aggregation. In order to study the evolution and nature of these aggregates as a function of pH, turbidity measurements were made. The turbidity $\tau_c$ of the dispersions was determined from their optical transmittance ($T$) at wavelength 800 nm with the relation $\tau_c = (\log_{10}(1/T))/lc$, where $c$ is the mass concentration of the silica in the dispersion, and $l$ is the optical path length. The transmittance of the samples was determined in 1 mm quartz cuvettes using a UV-vis spectrophotometer.

Another newly developed technique used for the characterization of aggregate morphology is the analytical photo-centrifuge. It allows speeding up the sedimentation of dispersions by the application of centrifugal force. The rate of sedimentation of nanoparticles or aggregates in the centrifugal field is dependent on their size and morphology. Hence monitoring sedimentation by measuring the intensity of the light transmitted through the sample can provide detailed information about the aggregate structure. As described elsewhere [17, 18], in Space and Time Extinction Profiles (STEP)-technology, the sample is measured simultaneously over its full sample length as a function of time as shown in Fig. 2.5. For a given type of sample cells the position corresponds to a defined sample volume, the relationship between position and sample volume can be established by calibration. This allows to directly determine separate phase volumes and to calculate packing densities.

In the present work, the analytical centrifugation measurements were carried out in cooperation with Prof. D. Lerche and Dr. T. Sobisch at LUM Berlin. The sedimentation kinetics and phase volume of the silica-protein hetero-flocculate, and the size distribution of the flocculated particles was derived from the progression of transmission profiles. The sedimentation kinetics was measured at a centrifugal acceleration of 36 g (bottom position). Subsequently, the compression kinetics of the sediments formed was obtained at 2,300 g. The size distributions were determined in a separate measurement in which the centrifugal acceleration was gradually increased from 13 to 2,300 g [19].

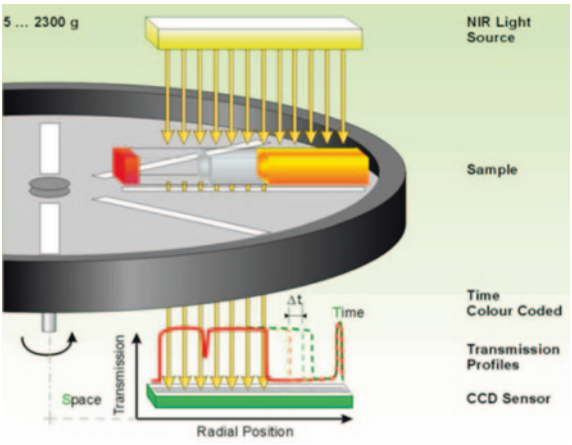


**Fig. 2.5** Experimental setup of the multisample analytical photocentrifuge. Parallel NIR-light is passed through the sample cells and the distribution of local transmission is recorded at preset time intervals over the entire sample length. (Figure reproduced with the permission of LUM, Berlin, GmbH)

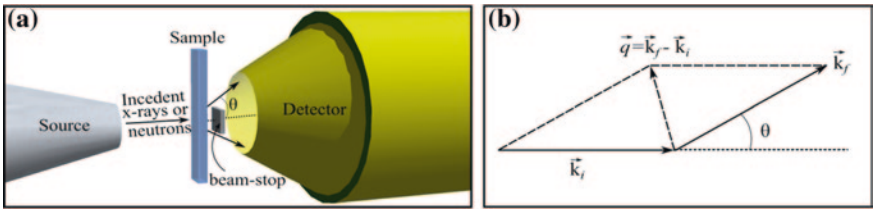


**Fig. 2.6** **a** Experimental setup for the small angle scattering experiment, where the incident beam from the source (neutron or X-ray) is projected on the sample and the scattered beam is monitored by the detector in line with the incident beam. **b** Schematic illustration of a neutron scattering geometry and vector relations

## 2.4 Small Angle Scattering

Scattering is the phenomenon where an incident radiation (light, X-rays or neutrons) is forced to deviate from a straight linear path when passing through a medium (solid, liquid or gas). In general, when an electromagnetic wave is incident on a system then the constituents of the system emit secondary wavelets in all the directions. The overall scattering pattern is then resulting from the superposition and interference of all the secondary wavelets. A typical set up for small angle instrument is shown in the Fig. 2.6a. Here, a collimated X-ray or neutron beam is incident on the sample and the pattern arising from the scattering was observed by the detector placed in line with the incident beam. Beam-stop is placed in order to avoid the high intensity direct beam, which could lead to damage of detector.

In my PhD work, Small Angle Neutron Scattering (SANS) and Small Angle X-ray Scattering (SAXS) were used to study the structural features of hard and soft matter in the nanoparticle dispersions. The principle of the two techniques is exactly the same but important differences between SANS and SAXS result from the different nature of the scattered radiation. Neutrons are neutral elementary subatomic particles which interact with the atomic nuclei of the sample. On the other hand, X-rays interact with the electron shell of the atoms and thus gives information about the electron density in different parts of the sample. In both cases, it is the elastic, coherent scattering of X-rays/neutrons that gives rise to small-angle scattering. Coherent scattering is "in phase" and thus can contribute to small-angle scattering. Incoherent scattering is isotropic in a small-angle scattering experiment and thus contributes to the background signal and degrades signal to noise [20]. Figure. 2.6b shows the scattering process in terms of incident ($k_i$) beam vector that scatters from a sample S at an angle $\theta$, resulting into secondary beam vector ($k_f$). For elastic, coherent scattering $\left|\overrightarrow{k_i}\right| = \left|\overrightarrow{k_f}\right|$, the scattering vector $q$ can be obtained as

$$\begin{aligned} q = |\vec{q}| &= \left|\overrightarrow{k_f} - \overrightarrow{k_i}\right| = \sqrt{k_f^2 + k_i^2 - 2k_i k_f \cos\theta} \\ &= \frac{4\pi}{\lambda}\sin\frac{\theta}{2} \end{aligned} \tag{2.9}$$

where λ is the wavelength of the incident beam and $\theta$ is the scattering angle.

Regardless of the fact that the sample is crystalline or amorphous, we can still write the condition for constructive interference in terms of Bragg's law:

$$2d\sin\frac{\theta}{2} = n\lambda \tag{2.10}$$

where $n$ is the order of peak (say $n = 1$), and $d$ is the real space distance corresponding to wave vector $q$ and is given by $d = 2\pi/q$. The formula between $q$ and $d$ gives the relation between the size of the object and the corresponding momentum transfer in a diffraction experiment. The measured counts (neutron or electron) of a scattered beam, $I(q)$, recorded by the detector in time $t$, is dependent on the absolute scattering cross section $\frac{\mathrm{d}\sum(q)}{\mathrm{d}\Omega}$, by the expression given by Eq. 2.11

$$I(q) = K_{inst} \times d \times t \times \mathrm{T} \times \frac{\mathrm{d}\sum(q)}{\mathrm{d}\Omega} \tag{2.11}$$

where $t$ is the counting time, $d$ is the sample thickness, T is the transmission of the sample and $K_{inst}$ is a constant dependent on instrumental factors and reads as

$$K_{inst} = \varphi_{\mathrm{flux}} \times \mathrm{A} \times \Delta\Omega \times \varepsilon \tag{2.12}$$

where $\varphi_{\mathrm{flux}}$ is the incident radiation flux on the sample (neutron/cm$^2$ s), A is the cross-sectional area of the incident beam, $\Delta\Omega$ is the solid angle subtended by the single pixel of the detector and $\varepsilon$ is the detector efficiency. The 2D data obtained for a sample is radial averaged to obtain the 1D data which is then treated for further instrumental correction to obtain the final reduced scattering profile $I(q)$ versus $q$, where $I(q)$ is expressed in the units of cm$^{-1}$ and $q$ in nm$^{-1}$ (or Å$^{-1}$).

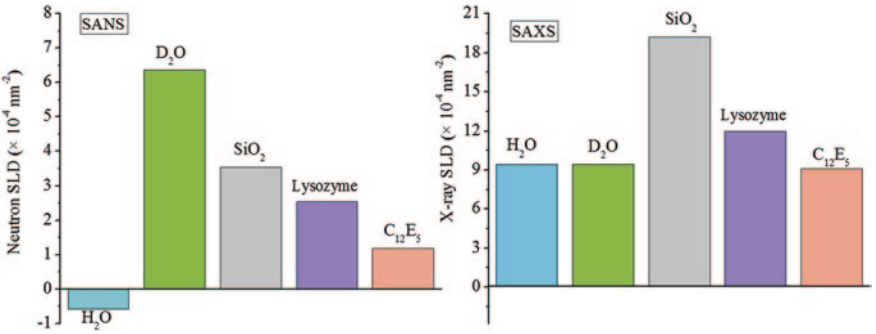


**Fig. 2.7** Scattering length density for different components used in the SAXS and SANS experiments. Neutron SLD for $H_2O$ is slightly negative while $D_2O$ has high positive value. This difference enables the use of $H_2O/D_2O$ mixture to contrast match other components in the dispersion, which is not possible with X-rays

The total scattering intensity from a dispersion of nanoparticles can be factorized as follows

$$I(q) = \varphi \Delta\rho^2 V P(q) S(q) \tag{2.13}$$

where $\varphi$ is the volume fraction of the scattering particles in the dispersion, $V$ is the volume of the single scattering particle, $\Delta\rho$ is the scattering contrast of the particle against the surrounding matrix, $P(q)$ is the form factor of a particle and $S(q)$ is the structure factor of the assembly of the particles. The scattering contrast $\Delta\rho$ in Eq. 2.13 is the difference between the Scattering Length Density (SLD) of scattering particles and the matrix. The value of $\rho$ for a sample composed of different atom $i$ can be calculated as [21]

$$\rho = \sum_i b_i \frac{\delta N_A}{m} = N \sum_i b_i \tag{2.14}$$

where $\delta$ is the bulk density of the molecule, $m$ is its relative molar mass, $N$ is the number density of scattering centers and $b_i$ is the coherent scattering length of the nucleus $i$ (for SANS). In X-ray scattering, the scattering length $b_i$ of an atom is proportional to the atomic number $Z_i$ and is given by $b_i = Z_i r_e$ [22], where $r_e$ is the classical electron radius $= 2.82 \times 10^{-15}$ m. Clearly, if in Eq. 2.13 $\Delta\rho$ is zero, the total scattering intensity $I(q)$ becomes zero. When this condition is met the scattering centers are said to be *contrast matched*. Since the scattering from a multi-component system is the weighted summation of the scattering contrast of each component, the contrast matching can simplify the scattering pattern. Figure 2.7 gives the neutron and Cu-$K_\alpha$ SLD [23] for $H_2O$, $D_2O$, silica, the protein lysozyme [24, 25] and the surfactant $C_{12}E_5$ (Chaps. 4 and 5). As can be seen, the SLD of $H_2O$ is <0 but for $D_2O$ it is >0. Hence in SANS, the key to the contrast is adjusting the volume ratio of $H_2O$ and $D_2O$ to arrive at the contrast match point for one of the dispersed components of a complex system (in our case silica). In SAXS, this zero scattering

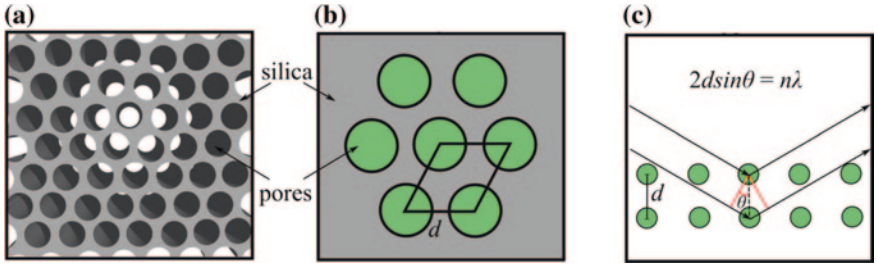


**Fig. 2.8** **a** Cartoon showing the ordered pores in the SBA-15 material; **b** 2D *hexagonal lattice* of the pores indicating the ordered lattice parameters. **c** Bragg's diffraction: Two beams with identical wavelength and phase (X-rays or neutrons) incident on an ordered solid, which are scattered off from two different pores within the lattice

condition cannot be achieved merely by $H_2O/D_2O$ mixture and the scattering pattern originates from all of its components. For investigating the effect of additives on the adsorbed surfactant on silica nano-spheres SANS measurements were performed on SANS-II instrument at the Paul Scherer Institut, Villigen, Switzerland. For avoiding complications, the silica dispersion was contrast matched by using $H_2O/D_2O$ ($\simeq$38:62) that corresponds to the SLD of pure silica ($=3.54 \times 10^{-4}$ nm$^{-2}$), hence the scattering originates solely from the surfactant in the dispersion. The SANS data reduction was done by using *BerSANS* software package [26]. Further modeling of the form factors and structure factor is explained in Chap. 3.

## 2.5 Small Angle Diffraction

In Chap. 5, we have studied the assembly of nonionic surfactant $C_{12}E_5$ in cylindrical mesopores of SBA-15 silica material. A given mesoporous material is identified by its pore diameter (or width) and pore lattice. A cylindrical pore is regarded as the unit cell i.e. the basic building block of the pseudo crystalline structure of SBA-15. Since the ordered structure of SBA-15 has hexagonal symmetry (Fig. 2.8a, b), the unit cell can be reduced to parallelepiped (Fig. 2.8b) that has two characteristic sides whose length is equal to '$d_{hk}$' lattice parameter. In our study of the self-assembly of surfactant in such ordered mesoporous silica materials, Small Angle Neutron Diffraction (SAND) was applied. The experimental setup of a SAD is similar to SAS. In both the cases, a beam of X-rays or neutrons is incident on the sample and the scattered or diffracted beam is measured by the detector. Diffracted waves from different centers in a material can interfere with each other and the resultant intensity distribution is strongly modulated by this interaction (Fig. 2.8c). If the scattering centers are arranged in a periodic fashion, as in crystals, the diffracted waves will consist of sharp interference maxima (peaks) with the same symmetry as the distribution of the scattering centers. The peaks in a diffraction pattern are directly related to the periodic distance between

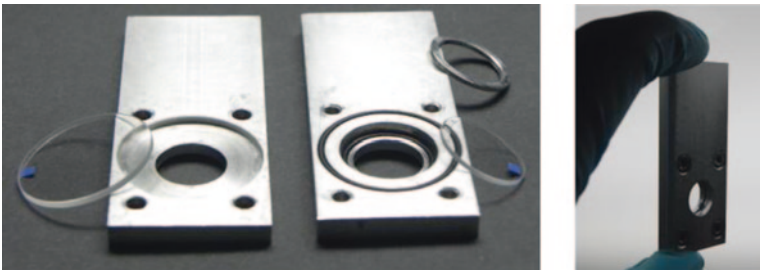

**Fig. 2.9** Sample holder used for the scattering experiments with SBA-15 in its disassembled and assembled stage

lattice planes $d_{hk}$ by Eq. 2.10. Whereas, the lattice parameter is related to the scattering vector (Eq. 2.9) by the following equation

$$d_{hk} = 4\pi\sqrt{h^2 + k^2 + hk}/q_{hk}\sqrt{3}, \quad hk = (10, 11, 20) \tag{2.15}$$

where $h$ and $k$ are the Miller indices of the diffraction peak maxima at the wave vector $q_{hk}$. Hence by determining the peak position in the SAD profile, the lattice parameter can be easily extracted.

SAND measurements were made on D16 instrument at Institut Laue-Langevin, Grenoble, France. 2-D Scattering data was acquired for two different detector angles 0 and 12°. The wavelength broadening for the instrument was $\Delta\lambda/\lambda = 0.1$. *LAMP* software was used for reducing 2D data into 1D diffraction curves, and *SciLab* was used for further modeling of the data. We have studied the adsorption of surfactants in SBA-15 by SAD of neutrons. The samples were prepared in the contrast match $H_2O/D_2O$ water at the contrast match point of SBA-15 ($3.70 \times 10^{-4}$ nm$^{-2}$), hence the scattering originates solely from the surfactant with no contribution from the silica material. In a typical experiment a fixed amount of SBA-15 material was taken in a vial with a fixed amount of contrast match water. A requisite amount of $C_{12}E_5$ surfactant was added to vial and was equilibrated for 12 h. After complete equilibration, SBA-15 with the adsorbed surfactant in the pores settles down and supernatant was drained away, leaving behind the thick slurry. This viscous slurry was transferred to the specially designed holders for the samples (as in Fig. 2.9) and was measured for SAND.

## References

1. Livage J, Sanchez C, Henry M, Doeuff S (1989) The chemistry of the sol-gel process. Solid State Ionics 32–33:633
2. Davis TM, Snyder MA, Krohn JE, Tsapatsis M (2006) Nanoparticles in lysine-silica sols. Chem Mater 18:5814
3. Thomassen LCJ, Aerts A, Rabolli V, Lison D, Gonzalez L, Kirsch-Volders M, Napierska D, Hoet PH, Kirschhock CEA, Martens JA (2010) Synthesis and characterization of stable monodisperse silica nanoparticle sols for in vitro cytotoxicity testing. Langmuir 26:328

4. Isrealachvilli JN (2011) Intermolecular and surface forces. Academic Press, USA
5. Atkins PW (1994) Physical chemistry. Oxford University Press, Oxford
6. Hunter RJ (1988) Zeta potential in colloid science: principles and applications. Academic Press, UK
7. Gregg SJ, Sing KSW (1982) Adsorption, surface area and porosity. Academic Press, UK
8. Chatoraj DK, Birdi KS (1984) Adsorption and the Gibbs surface excess. Plenum Press, USA
9. Findenegg GH (1992) Theoretical advancement in chromatography and related separation techniques. Kluwer Academic Publishers, The Netherlands
10. Dietsch O, Eltekov A, Bock H, Gubbins KE, Findenegg GH (2007) Crossover from normal to inverse temperature dependence in the adsorption of nonionic surfactants at hydrophilic surfaces and pore walls. J Phys Chem C 111:16045
11. Singh SK, Notely SM (2010) Adsorption of nonionic surfactants (CnEm) at the silica-water and cellulose-water interface. J Phys Chem B 114:14977
12. Lugo DM, Oberdisse J, Karg M, Schweins R, Findenegg GH (2009) Surface aggregate structure of nonionic surfactants on silica nanoparticles. Soft Matter 5:2928
13. Tyrode E, Ruthland MW, Bain CD (2008) Adsorption of CTAB on hydrophilic silica studied by linear and nonlinear optical spectroscopy. J Am Chem Soc 130:17434
14. Gu T, Zhu BY (1990) The S-type isotherm equation for adsorption of nonionic surfactants at the silica gel—water interface. Colloid Surf 44:81
15. Smith PK, Krong RI, Hermanson GT, Mallia AK, Gartner FH, Frovenzano MD, Fujimoto EK, Goeke NM, Olson BJ, Klenk DC (1985) Measurement of protein using bicinchoninic acid. Anal Biochem 150:76
16. Bharti B, Meissner J, Findenegg GH (2011) Aggregation of silica nanoparticles directed by adsorption of lysozyme. Langmuir 27:9823
17. Lerche D, Sobisch T (2007) Consolidation of concentrated dispersions of nano- and microparticles determined by analytical centrifugation. Powder Technol 174:46
18. Sobisch T, Lerche D (2008) Thickener performance traced by multisample analytical centrifugation. Colloid Surf A 331:114
19. Detloff T, Lerche D, Sobisch T (2006) Particle size distribution by space or time dependent extinction profiles obtained by analytical centrifugation. Part Part Syst Charact 23:184
20. Linder P, Zemb Th (2002) Neutrons, X-rays and light scattering methods applied to soft condensed matter. Delta Series-Elsevier, Netherlands
21. Gabrys BJ (2000) Applications of neutron scattering to soft condensed matter. Gordon and Beach Science publishers, USA
22. Narayanan J, Liu XY (2003) Protein interactions in undersaturated and supersaturated solutions: a study using light and X-ray scattering. Biophys J 84:523
23. http://www.ncnr.nist.gov/resources/sldcalc.html
24. Efimova YM, van Well AA, Hanefeld U, Wierczinski B, Bouwman WG (2004) On the neutron scattering length density of proteins in $H_2O/D_2O$. Phys B 350:e877
25. Stuhrmann HB, Fuess H (1976) A neutron small-angle scattering study of hen egg-white lysozyme. Acta Cryst A32:67
26. Keiderling U (2002) The new 'BerSANS-PC' software for reduction and treatment of small angle neutron scattering data. Appl Phys A 74:S1455

http://www.springer.com/978-3-319-07736-9

Adsorption, Aggregation and Structure Formation in Systems of Charged Particles
From Colloidal to Supracolloidal Assembly
Bharti, B.
2014, XVI, 150 p. 56 illus., 20 illus. in color., Hardcover
ISBN: 978-3-319-07736-9